

# Deformable Vessel-Based Registration Using Landmark-Guided Coherent Point Drift

Yipeng Hu, Erik-Jan Rijkhorst, Richard Manber, David Hawkes, and Dean Barratt

Centre for Medical Image Computing, University College London, London, UK

**Abstract.** Automatic, non-rigid registration of blood vessels (and other tubular structures) within a timescale suitable for use in image-guided surgical applications remains a significant challenge. We describe a novel approach to this problem in which an extension to the coherent point drift (CPD) algorithm is developed to enable landmarks, such as vessel bifurcations, to improve the registration accuracy and speed of execution. The new method – referred to as landmark-guided CPD (LGCPD) – is validated using vessels extracted from brain MRA and liver MR images, and is shown to be robust to missing vessel segments and noise, commonly encountered in realworld applications.

## 1 Introduction

Blood vessels, and other tubular structures, such as ducts, appear commonly in medical images. They can therefore provide very useful features for driving image registration schemes, particularly in image-guided surgical applications where knowledge of the location of blood vessels relative to surgical instruments is extremely important. Typical applications include neurosurgery, liver resection, liver transplant surgery, and vascular interventions where image guidance and registration technology is becoming increasingly relied upon to implement novel minimally-invasive techniques. Since vessels are distributed throughout organs, when they can be imaged, they provide a useful feature for capturing non-rigid deformation fields. However, modality-specific artefacts, organ deformation, missing vessel segments, and the different grey-level intensity characteristics of vessels imaged using different modalities mean that vessel-based registration in general remains a challenging task. This is particularly the case in the interventional setting where robustness, accuracy and speed are key criteria for clinical acceptance.

Vessel-based registration techniques have been reported for a number of research groups, principally those involving the liver or brain [1-4]. Many of the existing algorithms for vessel-based algorithms are feature-based approaches, which require prior segmentation of vessels and vessel centrelines [2;3]. Such methods have the advantage that the registration can often be performed very rapidly, but there is the additional overhead of the segmentation task, which may require manual interaction and can be subject to error. Intensity-based approaches, on the other hand, such as those described in [4-6] do not require prior image segmentation, are relatively computationally intensive, making them difficult to apply in many realtime

applications. Aylward et al. [1], Penney et al. [7] and Lange et al. [3] all combine feature- and image-intensity-based registration approaches.

Realtime, non-rigid vessel-based registration with little or no user interaction remains a significant challenge; Lange et al. [2;3] report a computation time of 10min for non-rigid registration, excluding the time taken to segment vessel images and manually identify bifurcations, whilst Reinersten et al. [4] report that registrations were completed within 1 minute. Both of these studies adopt thin-plate splines (TPS) to approximate the non-rigid component of the registration transformation that matches vessel centrelines. In this paper, we propose an alternative approach for fast, non-rigid vessel registration, based on the recently introduced coherent point drift (CPD) method [8]. In the CPD framework, it is assumed that the points in one dataset are generated by a mixture model centered on the points in the transformed dataset. The expectation maximization (EM) algorithm can then be used to solve the maximum likelihood estimation (MLE) problem, where the point correspondences and transformation are updated in the E and M steps, respectively. A solution from the calculus of variations is derived in [8] that allows efficient estimates of the regularised non-rigid transformation, where a regularisation term comes from a prior.

CPD has the advantage of flexibility since most existing general-purpose rigid and non-rigid point-based registration schemes can be formulated using the framework. In practice, however, CPD assumes no specific point correspondence other than the one derived from the Euclidean distances between points. As a result, it is insufficiently constrained in situations where, for example, physical constraints prevent certain types of deformation. In such cases, the likelihood function may not have a well-defined maximum. Furthermore, because the assumption of a Gaussian Mixture Model (GMM) may be inadequate or incorrect with imperfect data, leading to false global maxima in the likelihood function, the algorithm can be sensitive to the presence of outliers and/or missing data.

To address these limitations, we extend the original CPD algorithm so that explicitly defined, corresponding pairs of anatomical landmark points can be introduced, leading to improved behaviour and registration accuracy compared with the standard algorithm. Automatic registration of blood vessels using the *landmark-guided* CPD (LGCPD) algorithm is demonstrated using images of cerebral and liver vessels.

## 2 Methods

### 2.1 Vessel Segmentation

In this study, vessels to be registered were represented in two forms: a set of vessel surface points and a set of points that define the vessel centreline. These data were extracted from vessel images as follows: (1) the vessel image was first enhanced using an ITK implementation of a multi-scale vessel enhancing filter [9]. The outputs of this filter are a ‘vesselness’ image in which the intensity of each voxel provides a measure of the likelihood of a locally vessel-like feature being present in that voxel, and a 3D vector field, where the 3D local vessel direction vector is defined at each voxel [10]; (2) the vesselness image is converted to a binary volume,  $B$ , by applying a

user-defined threshold; (3) the surface pointset was sampled from the iso-surface computed from  $B$ ; (4) the centrelines were extracted from  $B$  using the 3D thinning, described in [11].

## 2.2 Coherent Point Drift Framework

The CPD method provides a framework for rigid and non-rigid alignment of two pointsets, where a target pointset is represented by ‘data’ vectors,  $\mathbf{x}_n$  ( $n=1,2,\dots,N$ ), and a source pointset is represented by ‘model’ vectors,  $\mathbf{y}_m$  ( $m=1,2,\dots,M$ ). Both vectors contain  $D$ -dimensional coordinates ( $D=3$  here). Each transformed model vector  $T(\mathbf{y}_m, \boldsymbol{\theta})$  is considered to contain the centroids of a set of Gaussians, where  $T$  is the spatial transformation of  $\mathbf{y}_m$  with transformation parameters  $\boldsymbol{\theta}$ . This pointset forms a mixture of  $M$  Gaussians with a weighted uniform distribution  $p(\mathbf{x}|m=M+1)=1/N$  (with scalar weight  $\omega$ ,  $0 \leq \omega \leq 1$ ) to explicitly account for outliers. The probability density function of the random vector  $\mathbf{x}$  is then given by:

$$p(\mathbf{x}) = \sum_{m=1}^{M+1} P(m) p(\mathbf{x} | m) = \omega \frac{1}{N} + (1 - \omega) \sum_{m=1}^M \frac{1}{M} G(\mathbf{x} | T(\mathbf{y}_m, \boldsymbol{\theta}), \sigma^2), \quad (1)$$

where the isotropic Gaussian distribution with parameter  $\sigma$  and mean vector  $\boldsymbol{\mu}$  is defined as  $G(\mathbf{x} | \boldsymbol{\mu}, \sigma^2) = (2\pi\sigma^2)^{-D/2} \exp(-\|\mathbf{x} - \boldsymbol{\mu}\|^2 / 2\sigma^2)$ . Given the pointset  $\mathbf{x}_n$ , representing the observed data, the following negative log-likelihood function for the parameters,  $\boldsymbol{\theta}$  and  $\sigma$ , can be used as an objective function and measure of the goodness of alignment:

$$E = -\sum_{n=1}^N \log p(\mathbf{x}_n) \quad (2)$$

Registration, which requires estimates of the transformation parameters, becomes a MLE problem and may be efficiently solved by the EM algorithm. The rigid or affine transformations are parameterised by a  $D$ -dimensional translation plus a  $D$ -dimensional rotation, or a  $D \times D$  unconstrained matrix, respectively. Closed-form solutions for these cases are derived in [8].

As explained in [8], an appropriate prior for a non-rigid transformation is  $P(v) = \exp(-(\lambda/2)\|Pv\|^2)$ , where  $v$  is a displacement function, which defines a non-rigid deformation field, and  $P$  is a linear operator that acts in this case as a high-pass filter. Using this prior, the objective function becomes  $E - \log(P(v)) = E + (\lambda/2)\|Pv\|^2$ . The EM algorithm can again be employed to solve this maximum a posterior problem so that 1) the E steps remain the same as in MLE; and 2) the negative complete log-likelihood function – the objective function to minimise in M steps – takes the following form:

$$Q(v, \sigma^2) = \frac{1}{2\sigma^2} \sum_{n=1}^N \sum_{m=1}^M P_{mn} \|\mathbf{x}_n - (\mathbf{y}_m + v(\mathbf{y}_m))\|^2 + \frac{NpD}{2} \log \sigma^2 + \frac{\lambda}{2} \|Pv\|^2, \quad (3)$$

where the terms independent of  $\sigma$  and  $v$  are ignored and  $Np = \sum_{n=1}^N \sum_{m=1}^M P_{mn}$ . The posterior probabilities,  $P_{mn}$  (also known as the responsibilities or membership probabilities) are computed in E steps, and are given by:

$$P_{mn} = P^{old}(m | \mathbf{x}_n) = \frac{\exp(-\frac{1}{2\sigma^2} \|\mathbf{x}_n - T(\mathbf{y}_m, \boldsymbol{\theta}^{old})\|^2)}{\sum_{k=1}^M \exp(-\frac{1}{2\sigma^2} \|\mathbf{x}_n - T(\mathbf{y}_k, \boldsymbol{\theta}^{old})\|^2) + (2\pi\sigma^2)^{D/2} \frac{\omega}{1-\omega} \frac{M}{N}}, \quad (4)$$

where  $\boldsymbol{\theta}^{old}$  are the parameters estimated in a previous iteration.

According to the calculus of variations approach and motion coherence theory [8], CPD chooses a Gaussian kernel with one parameter  $\beta$ , namely  $k(\mathbf{y}_i, \mathbf{y}_j) = \exp(-\|\mathbf{y}_i - \mathbf{y}_j\|^2 / 2\beta^2)$ . Thus, the optimal function form of  $v$  that minimises eq.(3) becomes a linear combination of the Gaussian kernel and  $M$  sets of  $D$ -dimensional coefficients. Therefore, the coefficients can be estimated by solving a linear least-squares problem and  $\sigma^2$  may be estimated by equating the corresponding derivative to zero. In [8], it is also suggested that a good minimum generally can be achieved with a single iteration of these two evaluations. A more detailed description of the solution and the implementation are omitted here for brevity, but can be found in [8].

### 2.3 Landmark-Guided Coherent Point Drift

In this section, we consider the situation where  $L$  additional landmark pairs are available to constrain the registration. In practice, such landmarks are treated differently from other vessel points. If  $\mathbf{x}_l^*$  and  $\mathbf{y}_l^*$  contain the co-ordinates of corresponding landmarks for  $l=1,2,\dots,L$ , we can in turn define a mathematically convenient prior over  $\boldsymbol{\theta}$  as the following joint probability of  $L$  Gaussians:

$$P(\boldsymbol{\theta} | \sigma^{*2}) = \prod_l^L G(\mathbf{x}_l^* | T(\mathbf{y}_l^*, \boldsymbol{\theta}), \sigma^{*2}) \quad (5)$$

where  $\sigma^{*2}$  is the new hyper-parameter, which controls the influence of the prior. Furthermore, in the non-rigid case, by assuming the independence between the known correspondence and the prior on the displacement field  $P(v)$ , the new “joint” prior may be given by:

$$P(v | \sigma^{*2}) = \prod_l^L G(\mathbf{x}_l^* | (\mathbf{y}_l^* + v(\mathbf{y}_l^*)), \sigma^{*2}) \cdot \exp(-\frac{\lambda}{2} \|Pv\|^2) \quad (6)$$

Therefore, the new objective function to minimise in  $M$  steps becomes:

$$Q^*(v, \sigma^2) = Q(v, \sigma^2) - \frac{\lambda}{2} \|Pv\|^2 - \log(P(v | \sigma^{*2})) \quad (7)$$

where  $Q$  is defined as in eq.(3). To obtain the transformation minimising eq.(7), the same approach described in Section 2.2 may be used. Taking the functional derivative of  $Q^*$ , so the independent terms may be omitted, gives:

$$\begin{aligned} \frac{\partial Q^*}{\partial v} &= \frac{\partial}{\partial v} \left[ \frac{1}{2\sigma^2} \sum_{n=1}^N \sum_{m=1}^M P_{mn} \|\mathbf{x}_n - (\mathbf{y}_m + v(\mathbf{y}_m))\|^2 + \frac{NpD}{2} \log \sigma^2 + \frac{\lambda}{2} \|Pv\|^2 \right. \\ &\quad \left. + \frac{1}{2\sigma^2} \sum_{l=1}^L \frac{\sigma^2}{\sigma^{*2}} \|\mathbf{x}_l^* - (\mathbf{y}_l^* + v(\mathbf{y}_l^*))\|^2 \right] \\ &= \frac{\partial}{\partial v} \left[ \frac{1}{2\sigma^2} \sum_{j=1}^{N+L} \sum_{i=1}^{M+L} P_{ij}^* \|\mathbf{x}_j - (\mathbf{y}_i + v(\mathbf{y}_i))\|^2 + \frac{NpD}{2} \log \sigma^2 + \frac{\lambda}{2} \|Pv\|^2 \right] \end{aligned} \quad (8)$$

$$\text{where, } P_{ij}^* = \begin{cases} P_{mn}, & (i = m, m \in [1, M]) \& (j = n, n \in [1, N]) \\ \sigma^2 / \sigma^{*2}, & (i = M + l) \& (j = N + l), l \in [1, L] \\ 0, & \text{otherwise} \end{cases}$$

$$\text{i.e. } [P_{ij}^*]_{(M+L) \times (N+L)} = \begin{bmatrix} [P_{mn}]_{M \times N} & \mathbf{0} \\ \mathbf{0} & \frac{\sigma^2}{\sigma^{*2}} \cdot \mathbf{I}_L \end{bmatrix},$$

$[\mathbf{x}_j]_{D \times (N+L)} = [\mathbf{x}_n]_{D \times N}, [\mathbf{x}_l^*]_{D \times L}$  and  $[\mathbf{y}_i]_{D \times (M+L)} = [\mathbf{y}_m]_{D \times M}, [\mathbf{y}_l^*]_{D \times L}$ . Eq.(4) can again be used to compute  $P_{mn}$  in E steps. As shown in the derivation of eq.(8), the new objective function has the same form of functional derivative as  $\partial Q / \partial v$ , so the same variational procedure to minimise  $Q$  given above may be used to minimise  $Q^*$ , with matrices  $[P_{mn}]$ ,  $[\mathbf{x}_n]$  and  $[\mathbf{y}_m]$  being replaced by  $[P_{ij}^*]$ ,  $[\mathbf{x}_j]$  and  $[\mathbf{y}_i]$ , respectively. The same procedure also applies for rigid and affine cases, where setting the partial derivatives of the objective function in M steps to zeros leads to direct solutions for  $\boldsymbol{\theta}$  and  $\sigma^2$ , subject to the same matrix replacements described as above. To update  $\sigma^2$ , equating the corresponding derivative to zero gives the estimator:

$$\hat{\sigma}^2 = \frac{1}{N \mathbf{p} D} \sum_{n=1}^N \sum_{m=1}^M \|x_n - (y_m + v(y_m))\|^2 \quad (9)$$

The original CPD has three parameters,  $\omega$ ,  $\lambda$  and  $\beta$ , controlling the influence of outliers, the amount of smoothness regularisation and strength of the points' mutual interaction, respectively. The additional parameter  $\sigma^*$  reflects the localisation error of the corresponding landmarks. The smaller the value is set for  $\sigma^{*2}$ , the stronger the constraints on the corresponding landmarks. In practice, this parameter can be adjusted depending on the spatial accuracy with which landmarks are defined.

## 2.4 Validation

In order to evaluate the performance of the LGCPD algorithm for vessel-based registration, experiments were performed using vessels extracted from one patient brain MR image, and two liver MR images, obtained on the same volunteer. A significant issue in validating registration algorithms is establishing an accurate gold standard transformation between images that is independent of the method under evaluation. In the first set of experiments, a finite element (FE) model was used to apply a physical deformation to a volume containing cerebral vessels, segmented from a brain MR images. This volume was used as the target volume, to which the original source volume was registered. This approach has the advantage that the voxel displacement field is known and can be compared directly with displacements estimated by the vessel-based registration. In a second experiment, an MR image of a liver was deformed using a displacement field generated by registering two MR images obtained at different phases of the breathing cycle. This displacement field was then applied to one of the MR images to generate a target image. Again, the displacement field is known, and therefore provides a “perfect” gold standard for validation.

### 2.4.1 Brain Vessel Deformation Using a Biomechanical Simulation

Using the method described in Section 2.1, surface and centreline points from a section of a cerebral blood vessel were extracted from a MR angiography (MRA) image of a consented patient who underwent neurosurgery at the National Hospital for Neurology and Neurosurgery, London. The voxel size of the MR volume  $0.49 \times 0.49 \times 0.7 \text{ mm}^3$ , and the image was acquired using a 3D TOF (MOTSA) sequence on a GE Signa Excite 1.5T scanner and an 8-channel SENSE phased-array head coil.

A tetrahedral mesh of the blood vessels was created from the binary image obtained by thresholding the vesselness image resulting from filtering the original MR image. This binary image was then labelled and imported to the MATLAB meshing interface tool, *iso2mesh* [12], which automatically constructs 3D solid tetrahedral meshes. As shown in Fig.1, a spherical region near to the vessel was included in the FE mesh to represent a region of interest (ROI), such as a tumour. The tissue region between the vessel and ROI was assumed to be homogeneous.

An anisotropic, nonlinear finite element (FE) solver [13] was used to simulate a physically plausible deformation of the vessel and tumour model. Displacement loads with a magnitude of 15 mm, in x, y and z directions, were applied to nodes within regions near the ends of the two vessel branches, while the other side of the mesh, near hepatic hilum, was left fixed. The tumour and surrounding tissue were assumed to be isotropic elastic materials described by a neo-Hookean model. The vessel wall was assumed to be a transversely isotropic, nonlinear material [13]. At each point along the vessel, transverse plane was defined as the plane orthogonal to the local vessel direction vector output from the vesselness filter. For the purposes of this study, all the isotropic materials were assumed to have a shear modulus of, 33.6kPa and 0.336kPa, and a bulk modulus of, 1.67GPa and 16.7kPa, for the ROI and surrounding tissue, respectively. The transverse isotropy for the vessel results in one extra stiffness parameter [13] which was set to 16.7kPa. Mesh node displacements were computed using the non-linear FE solver, described in [13] and implemented to run on a graphics processing unit (GPU).

The surface and centreline points defining the cerebral vessel were transformed into the deformed space by interpolating the FE nodal displacement field. The resulting points were considered as target points in the registrations. An additional rigid transformation was also applied before registration to test the algorithm.

### 2.4.2 Liver Vessel Deformation

To obtain a gold standard displacement field due to breathing motion from MR scans where the liver vasculature was clearly visible, two breath-hold MR volumes were registered using a fluid registration method [14]. This registration has been previously evaluated using real-time MR data and found to accurately model the respiratory liver motion [15]. The images were acquired on a healthy volunteer using a 1.5 T cylindrical bore Philips Achieva MR scanner at Guy's Hospital, London. The breath-hold scans were acquired at maximum exhale and mid-cycle with a field-of-view of  $400 \times 400 \times 270 \text{ mm}^3$  covering the whole abdomen. The voxel size was  $1.4 \times 1.4 \times 1.7 \text{ mm}^3$ .

For the liver vessels, vessel surface and centreline points were extracted as described above. The right hepatic vein was identified by manually defining one point within and finding all connected voxels from the binary representations of both the source and target images.

### 2.4.3 Registration Experiments

To investigate the effects of missing and noisy data on the vessel-based registration, the target (deformed) cerebral vessel pointsets were modified in the following ways: First, a 7mm segment from one branch was removed at a random position. Second, random anisotropic Gaussian noise with a variance of 1mm along the vessel and 9mm orthogonal to the vessel was added to the location of each target point. Third, the first two modifications were applied simultaneously. One hundred registrations were performed for each of the three cases using the original CPD method (without landmarks) and then the LGCPD method with three pairs of manually defined landmarks: one at the bifurcation and the one at each end of the two branches. The parameter values  $\sigma^*=0.01$ ,  $\omega=1$ ,  $\beta=1$  and  $\omega=0.1$  were used in all the experiments.

For the MR liver data, registrations were performed using the same parameter values, apart from a larger smoothness parameter of  $\beta=3$  due to the relatively noisy data. In LGCPD experiment, two pairs of landmarks were identified manually at two bifurcations, as shown in Fig.2.

To quantify the registration accuracy, a set of points were defined in the source images. For the cerebral vessel registration, the nodes inside the tumour and vessel surface points were used, whereas for the liver vessels the 3D volume surrounding the vessels was uniformly resampled. In each case, the displacement field produced by the CPD/LGCPD registration transformation was used to propagate the point coordinates into the target space. The target registration error (TRE) was calculated as the root-mean-square distances between point locations propagated using the CPD/LGCPD registration transformation versus using the gold standard displacement field (derived using a FE simulation or fluid registration for the cerebral and liver vessel images, respectively).

## 3 Results

An example of LGCPD versus CPD registration of the cerebral vessel is illustrated in Fig.1. The TRE results for all the cerebral vessel registrations are summarised in Table 1. The initial TREs for the vessel and the tumour before registration were 19.24 and 18.47 mm, respectively. Approximately 250 points were registered using the centreline representation, and 1000 using the surface representation. It can be seen from Table 1 that the LGCPD outperforms the CPD method in terms of registration accuracy. Furthermore, LGCPD registration using the centreline points was found to lead to a lower TRE for the tumour in all cases.

For the liver vessels, approximately 150 (250) and 300 (500) points were used for the source (target) centreline and surface representations, respectively. Fig.2 shows the result of registering these vessels. The TREs using the standard CPD method were 7.35 and 6.57mm using surface and centreline points, respectively, whereas these were improved to 5.51 and 2.60mm, respectively, by using LGCPD registrations. The initial TRE before registration was 14.12 mm. The TRE of a voxel as function of distance from the liver vessel surface is plotted in Fig.3. It was found that for any location with distance to the vessel surface smaller than 6.8mm, the TRE was smaller than 3mm. As the example shown in Fig.2, visual assessment of the registration results indicates incorrect correspondence found using the CPD method; in contrast,

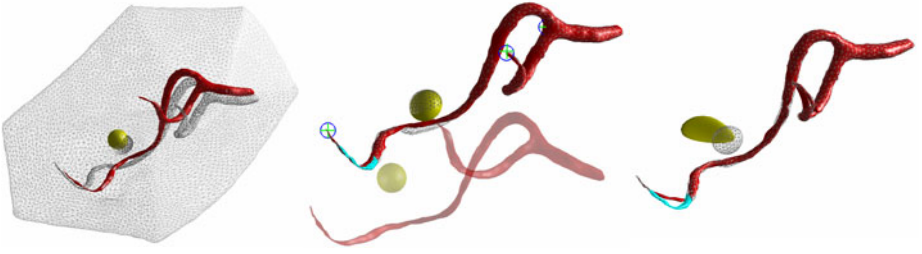


**Fig. 1.** Registration of a cerebral vessel (red), extracted from a patient MR image, to a deformed and corrupted version of itself (gray mesh). Left: The gray meshes represent the deformed vessel and tumour following a FE simulation. Middle: Example of the source vessel before and after registration using the LGCPD algorithm, shown in pink and red, respectively. Regions of the vessel removed to test the registration algorithm are shown in cyan, whilst the green crosses and blue circles indicate corresponding landmarks (bifurcations and ends of vessels). Right: Example of using the CPD registration algorithm without landmarks. It can be seen that, compared to the middle image, the alignment of the tumour and the ends of the longer branch are much less accurate.

**Table 1.** Summary of the TREs following registration of the cerebral vessels

TREs in mm (mean $\pm$ SD)		Missing Data		Noisy Data		Missing & Noisy Data	
		Vessel	ROI	Vessel	ROI	Vessel	ROI
CPD	Surface	2.88 $\pm$ 0.87	5.20 $\pm$ 1.59	1.15 $\pm$ 0.21	3.53 $\pm$ 1.60	2.51 $\pm$ 1.05	4.27 $\pm$ 1.75
	Centreline	3.02 $\pm$ 0.97	4.45 $\pm$ 1.81	2.40 $\pm$ 0.78	4.87 $\pm$ 2.05	3.43 $\pm$ 1.06	5.52 $\pm$ 2.51
LGCPD	Surface	0.80 $\pm$ 0.16	1.26 $\pm$ 0.37	0.63 $\pm$ 0.08	1.15 $\pm$ 0.23	0.87 $\pm$ 0.26	1.20 $\pm$ 0.27
	centreline	0.58 $\pm$ 0.18	0.54 $\pm$ 0.12	1.02 $\pm$ 0.18	1.05 $\pm$ 0.33	1.12 $\pm$ 0.22	1.10 $\pm$ 0.33

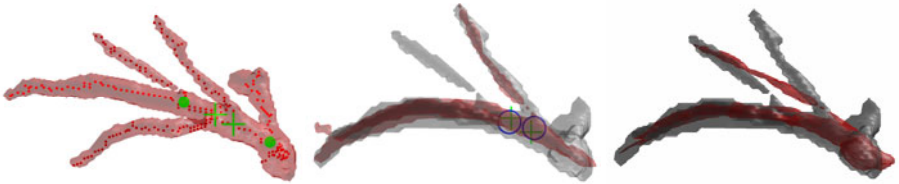


**Fig. 2.** Left: The right hepatic vein surface and centreline (shown in red) extracted from a deformed MR image of the liver. The bifurcations are denoted by green markers; the green crosses indicate the two landmarks used in the LGCPD registrations. Middle: example of a successful LGCPD registration showing the source vessel (red) aligned with the target vessel (gray). Corresponding landmarks (bifurcations) are shown as green crosses and blue circles. Right: Example of a CPD registration performed without using landmarks. It can be clearly seen that one source branch is aligned with the incorrect target branch.

the use of landmarks ensured that none of the LGCPD registrations produces such errors, both in the brain and liver cases.

Although the proposed LGCPD algorithm has the same computational complexity, and therefore speed, as the original CPD algorithm, it was found to execute faster in practice because fewer iterations were required to converge to a solution. In all the



experiments using our (unoptimised) implementation on a desktop PC with a 2.33GHz Intel® Core™ dual CPU processor and 3GB RAM, the centreline-based LGCPD registrations all converged within 1s. Registrations of the relatively larger number of vessel surface points were completed within 3s.

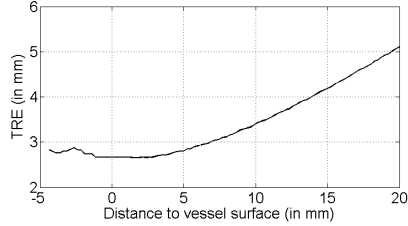


**Fig. 3.** Plot of the TREs of all voxels w.r.t. corresponding distances to the vessel surface (negative values indicate locations *inside* a vessel)

## 4 Discussion and Conclusions

In this paper, a new landmark-guided registration approach, based on the CPD algorithm, is proposed. The proposed method enables point landmarks to be incorporated in manner consistent with the original CPD formulation, resulting in an algorithm that is straightforward to implement, faster and more accurate than the original for vessel-based registration applications. Using centreline and surface point representation of vessels extracted from brain MRA and liver MR data, our results indicate that registrations can be performed within a few seconds, meaning that the method is highly appropriate for intraoperative applications, provided a method is employed that enables such representations to be generated in a similar timescale. A number of algorithms for automatic bifurcation identification and automatic vessel segmentation exist [16]. For the purpose of this study, all the landmarks were identified manually. One topic for further investigation is incorporation of a robust, automatic method to extract corresponding landmarks.

In this study, we used an unoptimised implementation of a well-known vesselness filter combined with simple thresholding and thinning to extract vessels and centreline points automatically. However, since all of these processes are parallelisable, significant speed-up in execution would be readily achievable using dedicated hardware. Furthermore, the algorithms could be optimised, for example, to limit the search space to regions near to vessels, or to utilise prior knowledge on likely vessel location and geometry from preoperative images or an initial slower registration, performed at the start of interventional procedure.

**Acknowledgments.** This work was supported by a UCL/UCLH Comprehensive Biomedical Research Centre New Initiative Project Grant (Ref. 96) and EPSRC Grant EP/F025750/1. Dean Barratt is funded by a Royal Academy of Engineering/EPSRC Research Fellowship. The Authors would like to thank Mr. Neil Kitchen and Dr. John Thornton from the National Hospital for Neurology & Neurosurgery, Dr. Freddy

Odille from UCL, and Prof. Tobias Schaefer from Imaging Sciences, King's College London for assistance in acquiring MR data for this study.

## References

1. Aylward, S.R., Jomier, J., Weeks, S., Bullitt, E.: Registration and Analysis of Vascular Images. *Int. J. Comput. Vision* 55(2-3), 123–138 (2003)
2. Lange, T., Eulenstein, S., Hunerbein, M., Schlag, P.M.: Vessel-based non-rigid registration of MR/CT and 3D ultrasound for navigation in liver surgery. *Computer Aided Surgery* 8(5), 228–240 (2003)
3. Lange, T., Papenberg, N., Heldmann, S., Modersitzki, J., Fischer, B., Lamecker, H., Schlag, P.: 3D ultrasound-CT registration of the liver using combined landmark-intensity information. *International Journal of Computer Assisted Radiology and Surgery* 4(1), 79–88 (2009)
4. Reinertsen, I., Descoteaux, M., Siddiqi, K., Collins, D.L.: Validation of vessel-based registration for correction of brain-shift. *Medical Image Analysis* 11(4), 374–388 (2007)
5. Hipwell, J.H., Penney, G.P., McLaughlin, R.A., Rhode, K., Summers, P., Cox, T.C., Byrne, J.V., Noble, J.A., Hawkes, D.J.: Intensity-based 2-D-3-D registration of cerebral angiograms. *IEEE Trans. Med. Imaging* 22(11), 1417–1426 (2003)
6. Slomka, P.J., Mandel, J., Downey, D., Fenster, A.: Evaluation of voxel-based registration of 3-D power Doppler ultrasound and 3-D magnetic resonance angiographic images of carotid arteries. *Ultrasound in Medicine & Biology* 27(7), 945–955 (2001)
7. Penney, G.P., Blackall, J.M., Hamady, M.S., Sabharwal, T., Adam, A., Hawkes, D.J.: Registration of freehand 3D ultrasound and magnetic resonance liver images. *Medical Image Analysis* 8(1), 81–91 (2004)
8. Myronenko, A., Song, X.: Point Set Registration: Coherent Point Drift. *IEEE Trans. on Pattern. Analysis. and Machine. Intelligence* (2010) (in press) (pre prints)
9. Mannesing, R., Viergever, M., Niessen, W.: Vessel enhancing diffusion: A scale space representation of vessel structures. *Medical Image Analysis* 10(6), 815–825 (2006)
10. Frangi, A., Niessen, W., Vincken, K., Viergever, M.: Multiscale vessel enhancement filtering. In: Wells, W.M., Colchester, A.C.F., Delp, S.L. (eds.) *MICCAI 1998. LNCS*, vol. 1496, pp. 130–137. Springer, Heidelberg (1998)
11. Homann, H.: Implementation of a 3D thinning algorithm. *Insight Journal* (2007)
12. Fang, Q., Boas, D.: Tetrahedral mesh generation from volumetric binary and gray-scale images. In: *Proceedings of the Sixth IEEE International Conference on Symposium on Biomedical Imaging: From Nano to Macro*, pp. 1142–1145. IEEE Press, Boston (2009)
13. Taylor, Z.A., Comas, O., Cheng, M., Passenger, J., Hawkes, D.J., Atkinson, D., Ourselin, S.: On modelling of anisotropic viscoelasticity for soft tissue simulation: Numerical solution and GPU execution. *Medical Image Analysis* 13(2), 234–244 (2009)
14. Crum, W.R., Tanner, C., Hawkes, D.J.: Anisotropic multi-scale fluid registration: evaluation in magnetic resonance breast imaging. *Phys. Med. Biol.* 50, 5153–5174 (2005)
15. Rijkhorst, E.J., Heanes, D., Odille, F., Hawkes, D., Barratt, D.: Simulating Dynamic Ultrasound using MR-derived Motion Models to assess Respiratory Synchronisation for Image-Guided Liver Interventions. In: Navab, N., Jannin, P. (eds.) *IPCAI 2010. LNCS*, vol. 6135, pp. 113–123. Springer, Heidelberg (2010)
16. Lesage, D., Angelini, E., Bloch, I., Funka-Lea, G.: A Review of 3D Vessel Lumen Segmentation Techniques: Models, Features and Extraction Schemes. *Medical Image Analysis* (2009)